

Impact of pH and chloride content on the biodegradation of magnesium alloys for medical implants: An in vitro and phase-field study. COMSOL implementation

Sasa Kovacevic^{a,*}, Wahaaj Ali^b, Tushar Kanti Mandal^a, Emilio Martínez-Pañeda^{a,*}, Javier LLorca^{b,c,*}

^a*Department of Engineering Science, University of Oxford, Oxford OX1 3PJ, UK*

^b*IMDEA Materials Institute, C/Eric Kandel 2, 28906 Getafe, Madrid, Spain*

^c*Department of Materials Science, Polytechnic University of Madrid, E.T.S. de Ingenieros de Caminos, 28040 Madrid, Spain*

Abstract

A variationally consistent phase-field model for assessing the degradation of Mg alloys in biological fluids is developed by Kovacevic et al. (2025) [1]. The model accurately predicts the corrosion performance of Mg alloys observed during the experiments, including their dependence on pH and chloride concentration. The capability of the framework to account for mechano-chemical effects during corrosion is demonstrated in practical orthopedic applications considering bioabsorbable Mg alloy implants for bone fracture fixation and porous scaffolds for bone tissue engineering. The strategy has the potential to assess the *in vitro* and *in vivo* service life of bioabsorbable Mg-based biomedical devices.

The theoretical formulation of the phase-field model is provided in the original paper [1], while this document provides instructions for its implementation in the finite element software COMSOL Multiphysics. Input files for different case studies are provided for demonstration purposes. If the code developed is used for research or industrial purposes, please cite:

S. Kovacevic, W. Ali, T.K. Mandal, E. Martínez-Pañeda, J. LLorca, Impact of pH and chloride content on the biodegradation of magnesium alloys for medical implants: An in vitro and phase-field study. Acta Biomater. 198 (2025) 546-565, <https://doi.org/10.1016/j.actbio.2025.03.034>.

Keywords: Corrosion, Corrosion kinetics, pH effects, Mechano-electrochemical coupled phase-field model

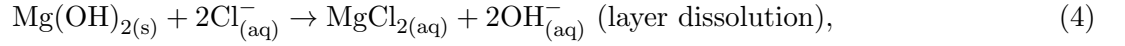
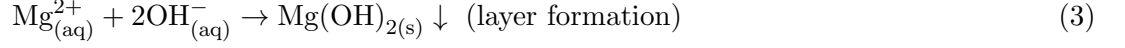
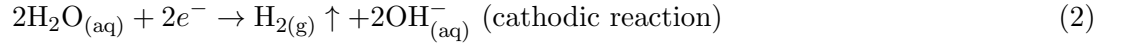
*Corresponding authors

Email addresses: sasa.kovacevic@eng.ox.ac.uk (Sasa Kovacevic), emilio.martinez-paneda@eng.ox.ac.uk (Emilio Martínez-Pañeda), javier.llorca@upm.es, javier.llorca@imdea.org (Javier LLorca)

1. The phase-field model of biocorrosion

1.1. Underlying electrochemistry

Magnesium dissolves in NaCl-based solutions via an electrochemical reaction with water



producing hydrogen gas and a porous corrosion product layer consisting of magnesium hydroxide ($\text{Mg}(\text{OH})_2$) that forms on the exposed metal surface. The layer initiates at regions on the metal surface where local concentrations of Mg^{2+} ions and hydroxide ions (OH^{-}) exceed the solubility product constant of $\text{Mg}(\text{OH})_2$. The formation rate of the $\text{Mg}(\text{OH})_2$ layer considerably depends on the synergistic effect of pH and concentration of aggressive Cl^{-} ions. The production of OH^{-} ions in Eq. (2) leads to an increase in pH that favors the formation and stabilization of the hydroxide layer, Eq. (3). However, the presence of Cl^{-} ions detains the formation of the corrosion product layer by increasing the solubility product constant of $\text{Mg}(\text{OH})_2$. The time required for this layer to form increases, leading to a faster corrosion rate. Cl^{-} ions also react with the corrosion layer and form highly soluble magnesium chloride (MgCl_2), Eq. (4). The hydroxide layer begins to dissolve and is prone to local breakdowns and thinning, creating layer-free areas that act as nuclei for localized (pitting) corrosion.

The bicarbonate buffer system maintains the pH by regulating the levels of carbonic acid (H_2CO_3), bicarbonate ions (HCO_3^{-}), and carbon dioxide (CO_2) via the following reaction



The production of hydrogen ions (H^{+}) controls the pH value. The $\text{Mg}(\text{OH})_2$ layer interacts with free CO_2 and produces Mg bicarbonate ($\text{Mg}(\text{HCO}_3)_2$), which is an unstable compound that quickly dissolves into Mg carbonate (MgCO_3).

1.2. Kinematics and thermodynamics

The system domain Ω comprises a biodegradable Mg alloy that acts as an electrode, an electrolyte that consists of positively and negatively charged aqueous ions, and a porous corrosion product layer that forms on the solid–liquid interface as the corrosion proceeds, Fig. 1. The following concentrations describe the surrounding environment and the reactions in Eqs. (1)–(6): the concentration of solidus species (Mg metal atoms) c_{Mg} present solely in the metal (electrode) and the concentration of ionic species present in the electrolyte $c_{\text{Mg}^{2+}}$, $c_{\text{OH}^{-}}$, and $c_{\text{Cl}^{-}}$. Albeit sodium ions (Na^{+}) are present in a NaCl-containing solution,

they are not included in the present model as they do not take part in Eqs. (1)–(6). The sensitivity of the formation of the hydroxide layer on Cl^- ions is implemented through the dependence of the solubility product constant of $\text{Mg}(\text{OH})_2$ on the chloride concentration, Section 1.5.

A continuous phase-field variable $\phi(\mathbf{x}, t)$ with a physical correspondence to the normalized Mg metal concentration $\phi = c_{\text{Mg}}V_m$ is introduced to distinguish different phases and for describing the evolution of the corroding front: $\phi = 1$ represents the solid phase (Mg alloy constituted only of Mg metal atoms), $\phi = 0$ corresponds to the liquid phase (corrosive medium with no Mg metal concentration), and $0 < \phi < 1$ indicates the thin interfacial region between the phases (solid–liquid interface) where the electrochemical reaction takes place. V_m denotes the molar volume of the material. To simplify notation, the ionic species considered are described by the set of dimensionless concentrations as $\vec{c} = \{\bar{c}_1 = c_{\text{Mg}^{2+}}/c_0, \bar{c}_2 = c_{\text{OH}^-}/c_0, \bar{c}_3 = c_{\text{Cl}^-}/c_0\}$, where c_0 stands for the standard bulk concentration of electrolyte solution. The underlying electrochemistry and corrosion mechanisms considered are schematically given in Fig. 1.

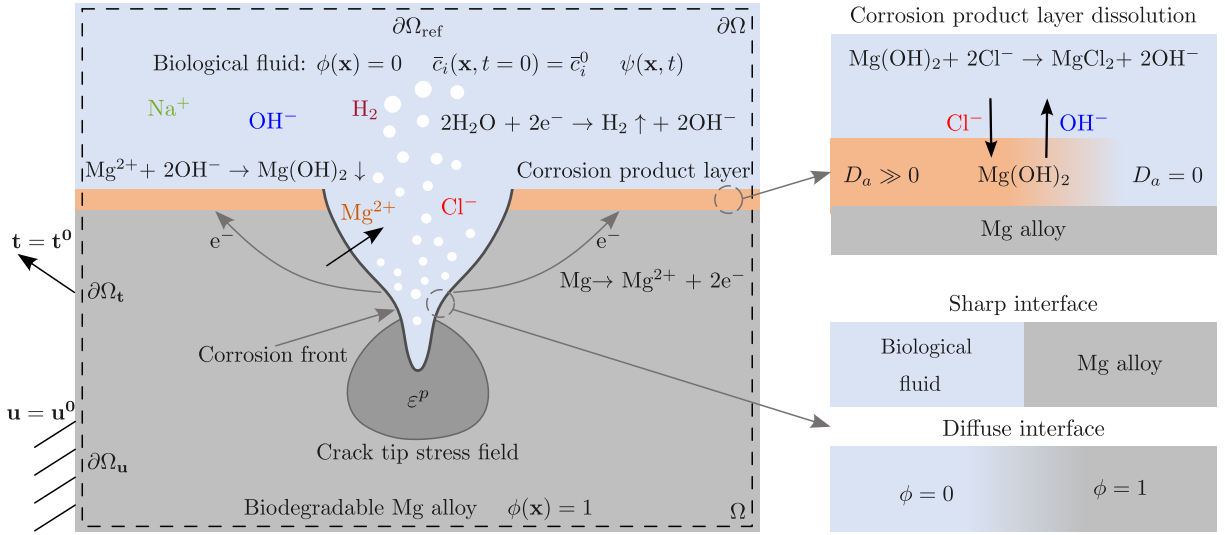


Figure 1: Underlying electrochemistry and diffuse interface description of the liquid (biological fluid $\phi = 0$) and solid (biodegradable Mg alloy $\phi = 1$) phases.

The free energy functional of the heterogeneous system in Fig. 1 includes the chemical $\mathcal{F}^{\text{chem}}$, electric $\mathcal{F}^{\text{elec}}$, gradient $\mathcal{F}^{\text{grad}}$, and mechanical $\mathcal{F}^{\text{mech}}$ free energy densities

$$\mathcal{F} = \int_{\Omega} \left[\mathcal{F}^{\text{chem}}(\vec{c}, \phi) + \mathcal{F}^{\text{elec}}(\vec{c}, \psi) + \mathcal{F}^{\text{grad}}(\nabla \phi) + \mathcal{F}^{\text{mech}}(\phi, \nabla \mathbf{u}) \right] d\Omega, \quad (7)$$

where $\mathbf{u}(\mathbf{x}, t)$ is the displacement vector to characterize the deformation of the material and $\psi(\mathbf{x}, t)$ the solution potential that arises due to uneven distributions of charged particles.

The total chemical free energy density $\mathcal{F}^{\text{chem}}$ is decomposed into the chemical free energy density associated with the ionic species present in solution and the double-well free energy density associated with the phase-field variable

$$\mathcal{F}^{\text{chem}}(\vec{c}, \phi) = c_0 RT \sum \bar{c}_i \ln \bar{c}_i + c_0 \sum \bar{c}_i \mu_i^{\ominus} + \omega g(\phi), \quad (8)$$

where R is the universal gas constant, T the absolute temperature (in Kelvin), μ_i^\ominus the reference molar chemical potential of ionic species i , and $g(\phi) = 16\phi^2(1-\phi)^2$ the double-well free energy function employed to describe the two equilibrium states for the solid ($\phi = 1$) and the liquid ($\phi = 0$) phases. ω in Eq. (8) is a constant that determines the energy barrier at $\phi = 1/2$ between the two minima at $\phi = 0$ and $\phi = 1$. The parameter ω is defined as $\omega = 3\Gamma/(4\ell)$, where Γ stands for the interfacial energy and ℓ the chosen nominal interface thickness.

The electric $\mathcal{F}^{\text{elec}}$ and interfacial $\mathcal{F}^{\text{grad}}$ free energy densities are commonly given as

$$\mathcal{F}^{\text{elec}}(\vec{c}, \psi) = c_0 F \psi \sum z_i \bar{c}_i \quad \mathcal{F}^{\text{grad}}(\nabla \phi) = \frac{1}{2} \kappa |\nabla \phi|^2, \quad (9)$$

where F is Faraday's constant, z_i the charge carried by component i , and $\kappa = 3\Gamma\ell/2$ the isotropic gradient energy coefficient.

The mechanical free energy density $\mathcal{F}^{\text{mech}}$ is only attributed to the solid phase ($\phi = 1$). Considering deformable elasto-plastic solids, the mechanical free energy density is additively decomposed into elastic $\mathcal{F}_e^{\text{mech}}$ and plastic $\mathcal{F}_p^{\text{mech}}$ components

$$\mathcal{F}^{\text{mech}}(\phi, \nabla \mathbf{u}) = h(\phi)(\mathcal{F}_e^{\text{mech}} + \mathcal{F}_p^{\text{mech}}), \quad (10)$$

where $h(\phi) = \phi^3(6\phi^2 - 15\phi + 10)$ acts as a degradation function to account for the transition from the uncorroded Mg alloy ($\phi = 1$) to the completely corroded phase ($\phi = 0$). The elastic and plastic strain energy densities are defined as

$$\mathcal{F}_e^{\text{mech}}(\nabla \mathbf{u}) = \frac{1}{2} \boldsymbol{\varepsilon}^e : \mathbf{C} : \boldsymbol{\varepsilon}^e \quad \mathcal{F}_p^{\text{mech}} = \frac{\sigma_y \varepsilon_0}{N+1} \left[\left(1 + \frac{\varepsilon^p}{\varepsilon_0} \right)^{N+1} - 1 \right], \quad (11)$$

where \mathbf{C} is the rank-four elastic stiffness tensor and $\boldsymbol{\varepsilon}^e = \boldsymbol{\varepsilon} - \boldsymbol{\varepsilon}^p$ is the elastic strain tensor obtained by subtracting the plastic strain tensor $\boldsymbol{\varepsilon}^p$ from the total strain tensor $\boldsymbol{\varepsilon} = 1/2(\nabla \mathbf{u} + (\nabla \mathbf{u})^T)$. The rank-four elastic stiffness tensor is described by the isotropic linear elasticity theory: $C_{ijkl} = \lambda \delta_{ij} \delta_{kl} + \mu(\delta_{ik} \delta_{jl} + \delta_{il} \delta_{jk})$, where λ and μ are Lamé elastic constants. The plastic part of mechanical free energy density for the intact solid $\mathcal{F}_p^{\text{mech}}$ in Eq. (11) is assumed to follow an isotropic power law hardening response with the von Mises theory of plasticity. Here, σ_y is the yield strength, ε_0 the onset of strain for hardening, N the hardening exponent, and $\varepsilon^p = \sqrt{2/3} \int_0^t |\dot{\boldsymbol{\varepsilon}}^p| dt$ the von Mises equivalent plastic strain.

1.3. Governing equations

The following time-dependent governing equations for the independent kinematic fields $\phi(\mathbf{x}, t)$, $\bar{c}_i(\mathbf{x}, t)$, $\psi(\mathbf{x}, t)$, and $\mathbf{u}(\mathbf{x}, t)$ are derived [1]

$$\left\{ \begin{array}{l} \frac{\partial \phi}{\partial t} = -L \left(\frac{\partial \mathcal{F}^{\text{chem}}}{\partial \phi} + \frac{\partial \mathcal{F}^{\text{mech}}}{\partial \phi} - \kappa \nabla^2 \phi \right) - \frac{i}{c_s F z} |\nabla \phi| \\ \frac{\partial \bar{c}_i}{\partial t} = -\nabla \cdot \mathbf{J}_i + R_i \\ \mathbf{J}_i = -M_i \nabla \left(\frac{\delta \mathcal{F}}{\delta \bar{c}_i} \right) = -D_i \left(\nabla \bar{c}_i + \frac{z_i F}{RT} \bar{c}_i \nabla \psi \right) \\ -\nabla \cdot (\xi \nabla \psi) = c_0 F \sum R_i z_i + Q \\ \nabla \cdot \boldsymbol{\sigma} = \mathbf{0} \end{array} \right\} \quad \text{in } \Omega, \quad (12)$$

complemented with boundary conditions

$$\left\{ \begin{array}{ll} \kappa \mathbf{n} \cdot \nabla \phi = 0 & \text{and} \quad \mathbf{n} \cdot \mathbf{J}_i = 0 \quad \text{on } \partial \Omega \\ \xi \mathbf{n} \cdot \nabla \psi = 0 & \text{on } \partial \Omega \quad \text{and} \quad \psi = \psi_{\text{ref}} \quad \text{on } \partial \Omega_{\text{ref}} \\ \mathbf{t} = \mathbf{n} \cdot \boldsymbol{\sigma} = \mathbf{t}^0 & \text{on } \partial \Omega_{\mathbf{t}} \quad \text{and} \quad \mathbf{u} = \mathbf{u}^0 \quad \text{on } \partial \Omega_{\mathbf{u}} \end{array} \right\}. \quad (13)$$

where ψ_{ref} is the solution potential on the reference electrode boundary $\partial \Omega_{\text{ref}}$, \mathbf{t}^0 and \mathbf{u}^0 are the prescribed traction and displacement vectors.

In the above equations, L stands for the mobility parameter that needs to be large enough to retain a constant interfacial thickness but small enough so that the convective term is not overly damped, \mathbf{J}_i the electrochemical flux, M_i the mobility parameter expressed using the Nernst-Einstein equation $M_i = D_i / (\partial^2 \mathcal{F}^{\text{chem}} / \partial \bar{c}_i^2)$, D_i the diffusion coefficient of ionic species i , $c_s = 1/V_m$ the site density of the Mg alloy, z the number of electrons involved in the electrochemical reaction ($z = 2$), $Q = c_0 F \mathbf{v} \cdot \nabla \phi$ the current generated by the electrochemical reaction at the corroding boundary, and $R_i = R'_i + R''_i$ the total reaction rates decomposed into the local electrochemical rates R'_i due to the anodic and cathodic reactions at the solid–liquid interface (Eqs. (1) and (2)) and the volumetric rates R''_i associated with the precipitation and dissolution of the corrosion product layer, Eqs. (3) and (4). R''_i also accounts for the production of H^+ ions and MgCO_3 in the case of the buffer solution, Eqs. (5) and (6). The current density of the mechanically deformed electrode i is written as [1]

$$i = i_a \exp\left(\frac{\alpha_a \sigma_h V_m}{RT}\right) \left(\frac{\varepsilon_p}{\varepsilon_0} + 1\right)^{\alpha_a} - i_c, \quad (14)$$

where $i_a = i_0 \exp(\alpha_a z F \eta / (RT))$ and $i_c = i_0 \exp(-(1 - \alpha_a) z F \eta / (RT))$ are the anodic and cathodic current densities of the non-deformed electrode, i_0 the exchange current density, α_a the anodic transfer coefficient, $\eta = \psi_s - \psi - \Delta \psi^{\text{eq}}$ the total overpotential of the non-deformed electrode, σ_h the hydrostatic stress, and ψ_s the potential of the metal ($\psi_s = 0$ V in this work). The equilibrium electrode-electrolyte potential

difference $\Delta\psi^{\text{eq}}$ is given as

$$\Delta\psi^{\text{eq}} = E^{\ominus} + 2.303 \frac{RT}{F} \text{pH} - \frac{RT}{zF} \ln \left(\frac{c_{\text{Mg}^{2+}}^s}{c_{\text{Mg}^{2+}}^b} \right), \quad (15)$$

where E^{\ominus} is the standard electrode potential difference between reactants and products, $c_{\text{Mg}^{2+}}^s$ the concentration of Mg^{2+} ions at the electrode surface (metal–electrolyte interface), $c_{\text{Mg}^{2+}}^b$ the concentration of Mg^{2+} ions in the bulk solution.

1.4. Reaction rates

The anodic reaction provides a source term for the evolution of Mg^{2+} ions while the cathodic reaction generates hydrogen gas and OH^- ions. Both reactions occur on the electrode surface and ascribe to the solid–liquid interface movement. The corresponding local reaction rates R'_i at the interface for each ionic species in the system are given as

$$R'_1 = -\frac{c_s}{c_0}(-\mathbf{v} \cdot \nabla \phi) = \frac{i}{c_0 F z} |\nabla \phi| \quad R'_2 = 2R'_1 \quad R'_3 = 0. \quad (16)$$

The expression for R'_1 implies that the amount of dissolved Mg-metal due to the electrochemical reaction is equivalent to the total amount of Mg^{2+} ions generated on the surface of the metal electrode. The second equation for R'_2 equates the amount of Mg^{2+} and OH^- ions produced at the solid–liquid interface according to Eqs. (1) and (2). Cl^- ions are not involved in the electrochemical reaction at the electrode surface, and thus, their interface reaction rates are equal to zero.

The volumetric reaction rate connected to the precipitation and dissolution of the corrosion product layer can be written as

$$R''_p = k_p(\bar{c}_1 \bar{c}_2^2 - \bar{K}_{\text{sp}}(\text{Cl}^-)) \quad R''_p = 0 \quad \text{if} \quad \bar{c}_1 \bar{c}_2^2 < \bar{K}_{\text{sp}}(\text{Cl}^-), \quad (17)$$

where $\bar{K}_{\text{sp}}(\text{Cl}^-) = K_{\text{sp}}(\text{Cl}^-)/c_0^3$ is the normalized solubility product constant of $\text{Mg}(\text{OH})_2$ and k_p the effective reaction rate responsible for the concurrent precipitation and dissolution of the $\text{Mg}(\text{OH})_2$ layer. The condition in the previous equation ensures that the precipitation reaction only occurs after the saturation is reached. The role of Cl^- ions in the precipitation of the corrosion product layer is included through the dependence of solubility product constant K_{sp} on chloride concentration. Mg^{2+} and OH^- ions produced at the solid–liquid interface due to the electrochemical reaction (16) are consumed with the production of the corrosion product $\text{Mg}(\text{OH})_2$ layer, Eq. (3). At the same time, a certain amount of Mg^{2+} and OH^- ions are released to solution due to the dissolution of the layer, Eq. (4). The consumption and release rates of these ions are controlled with the effective rate constant k_p . It is assumed here that MgCl_2 is unstable and instantaneously dissolves in Mg^{2+} and 2Cl^- , Eq. (4). This assumption eliminates tracking MgCl_2 as an independent concentration in the system. The amount of Cl^- ions annihilated during the dissolution of the layer is immediately released in solution due to rapid decomposition of MgCl_2 . The

concentration of Cl^- ions is thus unaltered under this assumption.

The volumetric reaction rates associated with the buffer system (Eqs. (5) and (6)) are expressed as

$$\begin{aligned} R''_{\text{pH}} &= k_{\text{pH}}(\bar{c}_2 - \bar{c}_2^{\text{lim}}) & R''_{\text{pH}} &= 0 \quad \text{if } \bar{c}_2 < \bar{c}_2^{\text{lim}} \\ R''_{\text{MgCO}_3} &= k_{\text{MgCO}_3}(\bar{c}_1 - \bar{c}_1^{\text{lim}}) & R''_{\text{MgCO}_3} &= 0 \quad \text{if } \bar{c}_1 < \bar{c}_1^{\text{lim}}. \end{aligned} \quad (18)$$

R''_{pH} accounts for the consumption of OH^- ions due to reaction (5) and limits the pH of solution. R''_{MgCO_3} is responsible for the consumption of Mg^{2+} ions due to the formation of MgCO_3 , Eq. (6). Here, \bar{c}_2^{lim} is the limit concentration of OH^- ions for a desired pH level of the solution. $\bar{c}_1^{\text{lim}} = c_{\text{MgCO}_3}/c_0$ stands for the threshold concentration of Mg^{2+} ions that must be reached to precipitate MgCO_3 . This threshold is defined in terms of the molar solubility of MgCO_3 , $c_{\text{MgCO}_3} = 2.4 \times 10^{-4}$ M. The condition ensures that the amount of Mg^{2+} ions below the solubility limit remains in solution, whereas any excess in Mg^{2+} ions beyond this limit is converted into MgCO_3 . k_{pH} and k_{MgCO_3} serve as a penalty for departing from the limit concentrations \bar{c}_1^{lim} and \bar{c}_2^{lim} . They must be large enough to enforce the equilibrium but not to obstruct the simulation. Combining Eqs. (17) and (18), the volumetric reaction rates for each ionic species are given as

$$R''_1 = -R''_p - R''_{\text{MgCO}_3} \quad R''_2 = 2R''_p - R''_{\text{pH}} \quad R''_3 = 0. \quad (19)$$

Although there are no reaction rates associated with Cl^- ions in the present model ($R'_3 = R''_3 = 0$), they influence corrosion kinetics through the solubility product constant.

1.5. Dependence of solubility product constant on the chloride concentration

The solubility product constant K_{sp} determines the starting point of corrosion layer precipitation initiation. A lower value of the solubility product constant shortens the time required for the formation of the layer. In the present investigation, the dependence of K_{sp} on the chloride concentration is expressed by following experimental data on the solubility of $\text{Mg}(\text{OH})_2$ in Cl^- ions containing solutions

$$K_{\text{sp}}(\text{Cl}^-) = K_{\text{sp}}^{1\text{M}} + B \log_{10}[\text{Cl}^-], \quad (20)$$

where $K_{\text{sp}}^{1\text{M}} = 1.24 \times 10^{-10} \text{ mol}^3/\text{L}^3$ is the solubility product constant in 1 M Cl^- and $B = 4.61 \times 10^{-11} \text{ mol}^3/\text{L}^3$ is a constant obtained through the fitting against experimental data. Here, $[\text{Cl}^-]$ denotes the molar concentration of Cl^- ions. The thermodynamic equilibrium equation for the precipitation of the hydroxide layer (Eq. (3)) can be written as

$$\log_{10}[\text{Mg}^{2+}] + 2\log_{10}[\text{OH}^-] = \log_{10}K_{\text{sp}}(\text{Cl}^-) \quad \log_{10}[\text{Mg}^{2+}] = 28 - 2\text{pH} + \log_{10}K_{\text{sp}}(\text{Cl}^-), \quad (21)$$

where $-\log_{10}[\text{OH}^-] = 14 - \text{pH}$. $[\text{Mg}^{2+}]$ and $[\text{OH}^-]$ denote the molar concentration of Mg^{2+} and OH^- ions. The dependence of the solubility product constant and chemical stability diagram on the chloride concentration is depicted in Fig. 2. The inset in Fig. 2(a) shows the variation in the solubility product

constant K_{sp} for the range of chlorine concentration considered in the current work and in common corrosive media used in Mg corrosion tests for biomedical applications. As indicated in Fig. 2, a variation in chloride concentration from 52 mM Cl^- to 156 mM Cl^- has a negligible effect on the solubility product constant K_{sp} and the equilibrium condition for the precipitation of $\text{Mg}(\text{OH})_2$ layer. This observation is experimentally validated in the current investigation, as discussed in the following section.

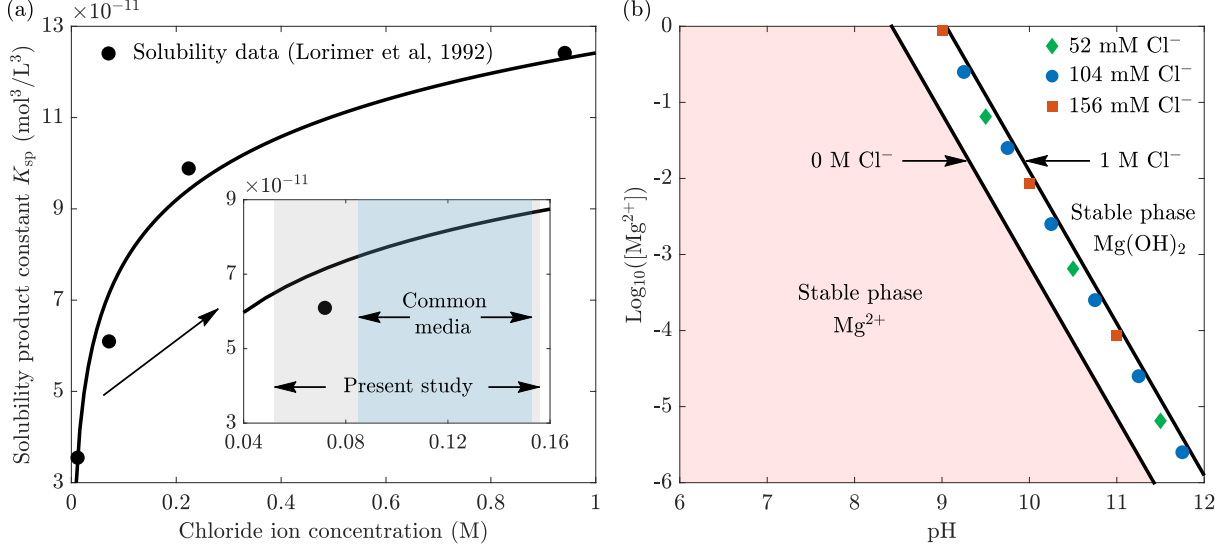


Figure 2: Dependence of (a) solubility product constant K_{sp} and (b) chemical stability diagram on the concentration of chloride ions. The light grey and blue areas stand for the range of chloride ion concentration used in the present study and in common corrosive media for Mg corrosion tests for biomedical applications. $[\text{Mg}^{2+}]$ denotes the molar concentration of Mg^{2+} ions.

1.6. Dimensional analysis

The resulting set of governing equations is normalized using the interface thickness ℓ as the characteristic length, the diffusion coefficients of Mg^{2+} ions D_1 , and the energy barrier ω as the reference energy density. They render the following set of nondimensional governing equations

$$\left\{ \begin{array}{l} \frac{\partial \phi}{\partial \bar{t}} = -\tau \left(\frac{\partial \bar{\mathcal{F}}^{\text{chem}}}{\partial \phi} + \frac{\partial \bar{\mathcal{F}}^{\text{mech}}}{\partial \phi} - \bar{\kappa} \bar{\nabla}^2 \phi \right) - P_e |\bar{\nabla} \phi| \\ \frac{\partial \bar{c}_i}{\partial \bar{t}} = \bar{\nabla} \cdot \left[\bar{D}_i (\bar{\nabla} \bar{c}_i + z_i \bar{c}_i \bar{\nabla} \bar{\psi}) \right] + \bar{R}'_i + \bar{R}''_i \\ - \bar{\nabla} \cdot (\bar{\xi}_l \bar{\nabla} \bar{\psi}) = \sum \bar{R}_i z_i + P_e |\bar{\nabla} \phi| \\ \bar{\nabla} \cdot \bar{\sigma} = 0 \end{array} \right\} \quad \text{in } \Omega, \quad (22)$$

along with the corresponding nondimensional boundary conditions. In the previous equation, $\bar{t} = tD_1/\ell^2$, $\bar{\mathbf{x}} = \mathbf{x}/\ell$, $\bar{\nabla} = \ell \nabla$, $\bar{\mathcal{F}}^{\text{chem}} = \mathcal{F}^{\text{chem}}/\omega$, $\bar{\mathcal{F}}^{\text{mech}} = \mathcal{F}^{\text{mech}}/\omega$, $\bar{\kappa} = \kappa/(\omega \ell^2)$, $\bar{D}_i = D_i/D_1$, $\bar{\psi} = \psi F/(RT)$, $\bar{\xi}_l = \xi_l RT/(D_1 c_0 F^2)$, and $\bar{\sigma} = \sigma/\omega$. The nondimensionalized reaction rates are defined as

$$\begin{aligned} \bar{R}'_1 &= \frac{c_s}{c_0} P_e |\bar{\nabla} \phi| & \bar{R}'_2 &= 2\bar{R}'_1 & \bar{R}'_3 &= 0 \\ \bar{R}''_1 &= -\bar{R}''_p - \bar{R}''_{\text{MgCO}_3} & \bar{R}''_2 &= 2\bar{R}''_p - \bar{R}''_{\text{pH}} & \bar{R}''_3 &= 0 \\ \bar{R}''_p &= D_a (\bar{c}_1 \bar{c}_2^2 - \bar{K}_{sp}(\text{Cl}^-)) & \bar{R}''_{\text{pH}} &= \bar{k}_{\text{pH}} (\bar{c}_2 - \bar{c}_2^{\text{lim}}) & \bar{R}''_{\text{MgCO}_3} &= \bar{k}_{\text{MgCO}_3} (\bar{c}_1 - \bar{c}_1^{\text{lim}}). \end{aligned} \quad (23)$$

The characteristic times for diffusion of ions within the bulk solution t_d , interface migration due to the interfacial energy reduction t_ϕ , interface motion due to the electrochemical reaction t_v , volumetric reaction rate for the precipitation/dissolution of the corrosion product layer t_{k_p} are

$$t_d = \frac{\ell^2}{D_1^l} \quad t_\phi = \frac{1}{L\omega} \quad t_v = \frac{\ell}{v} \quad t_{k_p} = \frac{1}{k_p}, \quad (24)$$

where $v = |\mathbf{v}| = i/(c_s F z)$ is the magnitude of the interface velocity due to the electrochemical reaction. The relative strength of convection, diffusion, and reactions is represented by the following dimensionless numbers

$$\tau_\phi = \frac{t_v}{t_\phi} \quad P_e = \frac{t_d}{t_v} \quad \tau = \frac{t_d}{t_\phi} = P_e \tau_\phi \quad D_a = \frac{t_d}{t_{k_p}}. \quad (25)$$

The rate of material transport at the interface is controlled by τ_ϕ , τ , and the Peclet number P_e while the effective reaction kinetics for the formation/dissolution of the corrosion product layer is governed by the Damköhler number D_a . The interface migration is dominantly governed by the electrochemical reaction at the solid–liquid interface compared to the diffusion part in Eq. (12). τ_ϕ is the ratio between convective and diffusive transport of the phase-field variable. As the interface is governed by the electrochemical reaction, the condition $\tau_\phi \ll 1$ provides the criterion for the interfacial mobility coefficient that reads $L \ll v/(\ell\omega)$. The ratio between bulk diffusion and interface diffusion is controlled by τ . As the characteristic time for interface diffusion is large, it is expected that $\tau = P_e \tau_\phi \ll 1$.

The Peclet number P_e determines the rate-limiting process for material transport between bulk diffusion and the electrochemical reaction at the interface. When $P_e \gg 1$, the electrochemical reaction is much faster than the diffusion and the process is driven by bulk diffusion (diffusion-controlled corrosion). For $P_e \ll 1$, diffusion is faster than the electrochemical reaction such that there is no accumulation of species at the solid–liquid interface (activation-controlled corrosion). Two extreme scenarios are possible regarding the volumetric reaction kinetics ascribed to the formation/dissolution of the $\text{Mg}(\text{OH})_2$ layer. $D_a = 0$ implies that the layer does not form (the formation and dissolution rates are equal) and that all Mg^{2+} and OH^- ions generated in (16) stay within the electrolyte. For $D_a \gg 0$ the formation rate dominates and the layer nucleates. $D_a < 0$ is not physical as it would imply that dissolution occurs faster than formation. Hence, $D_a \gg 0$ is enforced in this investigation and its value is determined through the fitting against the experimental measurements on the concentration of Mg^{2+} ions in the solution. \bar{k}_{pH} and \bar{k}_{MgCO_3} in Eq. (23) are the normalized penalty coefficients that enforce the limit concentrations associated with the buffer system.

2. COMSOL implementation

The resulting governing equations and accompanying boundary conditions are solved using the finite element software COMSOL Multiphysics [2]. To demonstrate the model implementation in COMSOL Multiphysics two different case studies are considered: Mg wires immersed in buffer-free and buffer-

controlled NaCl solutions.

The numerical simulation is conducted by considering a one-dimensional axisymmetric domain as depicted in Fig. 3. The actual diameter of the wire utilized in the experiments, $d = 0.30$ mm, is considered in the simulation. To accurately reflect the experimental conditions, the size of the electrolyte is determined by preserving the volume ratio between the Mg alloy and the amount of solution used in the degradation tests. Using the dimensions of the wire, a total of 50 mL of solution, and assuming the electrolyte has a cylindrical shape, it is found that the equivalent radius of the electrolyte is approximately $217d$, Fig. 3. The nondimensional form of governing equations (12) is solved with accompanying initial and boundary conditions for each primary field variable. The initial concentration values of each ionic species are based on the experimental setup. The initial concentration of Mg^{2+} ions in the domain is set to zero. A pH of 5.5 is used to calculate the initial concentrations of OH^- ions. The initial concentration of Cl^- ions in the medium matches the values used in the experiment. A zero-flux boundary condition for the diffusion of all ionic species and phase-field variable is enforced at the outer boundaries of the domain to resemble the closed environment of the *in vitro* experiments. This boundary condition ensures that no diffusion occurs across the domain boundary. A zero reference solution potential is imposed on the far right boundary in the electrolyte. The remaining boundaries are treated as perfectly isolated with no flux boundary condition for the solution potential.

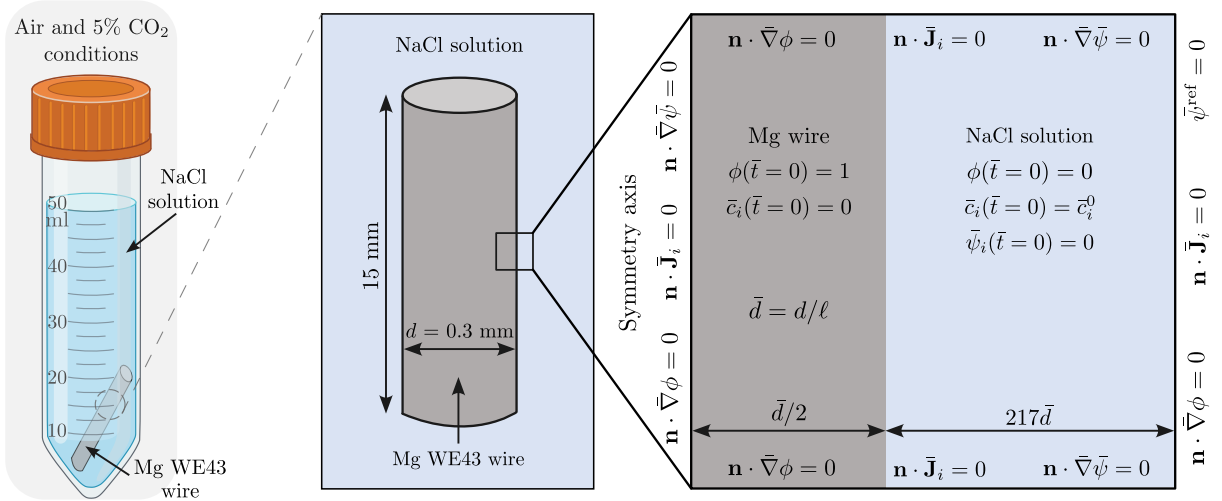


Figure 3: Schematic representation of the experimental setup (left) and the corresponding nondimensional computational domain (right) for the Mg alloy wire immersed in different NaCl solutions.

The material properties of the metal and the diffusivity of ions used in the simulation are listed in Table 1. For consistency with experimental observations, the standard electrode equilibrium potential E^θ and the electric conductivity of the electrolyte ξ are made dependent on chloride concentrations. E^θ is estimated from potentiodynamic polarization curves and is set to $E^\theta = -1.20$ V (vs. SHE) for the reference solution of 104 mM NaCl. For the 52 mM NaCl and 156 mM NaCl solutions, the values are set to $E^\theta = -1.1975$ V (vs. SHE) and $E^\theta = -1.2025$ V (vs. SHE) following reported variations in the literature. The electric conductivity of the electrolyte is set to $\xi = 0.52$ S/m for 52 mM NaCl, $\xi = 1$ S/m for 104 mM NaCl, and $\xi = 1.375$ S/m for 156 mM NaCl. The anodic charge transfer coefficient α_a is estimated

Quantity	Value	Unit
Absolute temperature T	310.15	K
Molar volume of magnesium V_m	13.998	cm ³ /mol
Diffusion coefficient of Mg ²⁺ ions D_1	7.06×10^{-10}	m ² /s
Diffusion coefficient of OH ⁻ ions D_2	5.273×10^{-9}	m ² /s
Diffusion coefficient of Cl ⁻ ions D_3	2.032×10^{-9}	m ² /s
Standard concentration in the electrolyte c_0	1	mol/L
Interfacial energy Γ	0.5	J/m ²
Anodic charge transfer coefficient α_a	0.30	-

Table 1: Parameters used in all phase-field simulations.

from potentiodynamic polarization curves. It is assumed to be independent of chloride concentration and set to $\alpha_a = 0.30$. The normalized solubility product constant \bar{K}_{sp} is defined using Eq. (29). The charge numbers of ionic species considered z_i have common values, as stated in Eqs. (1)–(4). The phase-field model parameters ω (Eq. (8)) and κ (Eq. (9)) are related to the interfacial energy Γ and the nominal chosen interface thickness ℓ . The interface thickness is set to be significantly smaller than the characteristic domain size ($\ell = 5 \mu\text{m}$). The simulation for model calibration and validation assumes uniform corrosion and the mechanical effect (Eq. (14)) is not considered.

Three additional parameters need to be specified: the exchange current density i_0 , the reaction rate for the formation/dissolution of the corrosion product layer D_a , and the phase-field mobility parameter L . The exchange current density is a physical parameter that depends on the pH and temperature of the solution. Due to a lack of experimental data on this parameter in NaCl solutions and at the temperature considered, the exchange current density is determined by fitting against experimental measurements. The same fitting approach is applied to the Damköhler number D_a . The phase-field mobility parameter L is selected based on dimensional analysis such that the condition $L \ll v/(\ell\omega)$ is satisfied. $L = v/(10\ell\omega)$ is used in the present investigation. These three parameters are the same for the air and 5% CO₂ environments. To enforce the buffer effects, the penalty coefficients \bar{k}_{pH} and \bar{k}_{MgCO_3} need to be defined. They should be chosen large enough to enforce equilibrium conditions (23). While larger values achieve equilibrium more quickly, they can significantly increase computational costs by reducing the time step and potentially cause convergence issues. Hence, they should be selected judiciously. In the present study, the penalty coefficients are set to $\bar{k}_{pH} = 1$ and $\bar{k}_{MgCO_3} = 10$ as a trade-off between accuracy and computational efficiency. Under the assumed condition for L and adopted anodic charge transfer and penalty coefficients, the current model has only two parameters that need to be fitted against experimental data: the exchange current density i_0 and the Damköhler number D_a for both buffer-free and buffer-controlled media.

The governing equations for these two case studies (in the absence of mechanical loading) are

$$\left\{ \begin{array}{l} \frac{\partial \phi}{\partial t} = -\tau \left(\frac{\partial \bar{\mathcal{F}}^{\text{chem}}}{\partial \phi} - \bar{\kappa} \bar{\nabla}^2 \phi \right) - P_e |\bar{\nabla} \phi| \\ \frac{\partial \bar{c}_i}{\partial t} = \bar{\nabla} \cdot \left[\bar{D}_i (\bar{\nabla} \bar{c}_i + z_i \bar{c}_i \bar{\nabla} \bar{\psi}) \right] + \bar{R}'_i + \bar{R}''_i \\ - \bar{\nabla} \cdot (\bar{\xi}_l \bar{\nabla} \bar{\psi}) = \sum \bar{R}_i z_i + P_e |\bar{\nabla} \phi| \end{array} \right\} \quad \text{in } \Omega. \quad (26)$$

The primal kinematic variables are the phase field order parameter ϕ , concentration of each species i \bar{c}_i , and the solution potential ψ . The **Mathematics** module with the **General Form** PDE interfaces is used to describe all the equations [3].

The **General Form** PDE interface in the following form is used for the phase-field equation

$$e_a \frac{\partial^2 \phi}{\partial t^2} + d_a \frac{\partial \phi}{\partial t} + \nabla \cdot \Gamma = f \quad (27)$$

where the coefficients are set to $d_a = 1$ and $e_a = 0$. The r and z components of the Γ vector are given as

$$\begin{aligned} \Gamma_r &= -\tau \bar{\kappa} \frac{\partial \phi}{\partial r} \\ \Gamma_z &= -\tau \bar{\kappa} \frac{\partial \phi}{\partial z} \end{aligned} \quad (28)$$

while the source term f includes the following term

$$f = -\tau \bar{\omega} g'(\phi) - P_e |\bar{\nabla} \phi| - \frac{\Gamma_r}{r}. \quad (29)$$

The last term in the previous expression accounts for the divergence operator in axisymmetric coordinates.

The **General Form** PDE interface in the following form is used for the diffusion equation of each ionic species

$$e_a \frac{\partial^2 \bar{c}_i}{\partial t^2} + d_a \frac{\partial \bar{c}_i}{\partial t} + \nabla \cdot \Gamma = f \quad (30)$$

where the coefficients are set to $d_a = 1$ and $e_a = 0$. The r and z components of the Γ vector are given as

$$\begin{aligned} \Gamma_r &= -\bar{D}_i \left(\frac{\partial \bar{c}_i}{\partial r} + z_i \bar{c}_i \frac{\partial \bar{\psi}}{\partial r} \right) \\ \Gamma_z &= -\bar{D}_i \left(\frac{\partial \bar{c}_i}{\partial z} + z_i \bar{c}_i \frac{\partial \bar{\psi}}{\partial z} \right) \end{aligned} \quad (31)$$

while the source term f includes the following term

$$f = \bar{R}'_i + \bar{R}''_i - \frac{\Gamma_r}{r}. \quad (32)$$

The last term in the previous expression accounts for the divergence operator in axisymmetric coordinates.

The **General Form** PDE interface in the following form is used for the solution potential distribution equation

$$e_a \frac{\partial^2 \bar{\psi}}{\partial t^2} + d_a \frac{\partial \bar{\psi}}{\partial t} + \nabla \cdot \Gamma = f \quad (33)$$

where the coefficients are set to $d_a = 0$ and $e_a = 0$. The r and z components of the Γ vector are given as

$$\begin{aligned} \Gamma_r &= -\bar{\xi}_l \frac{\partial \bar{\psi}}{\partial r} \\ \Gamma_z &= -\bar{\xi}_l \frac{\partial \bar{\psi}}{\partial z} \end{aligned} \quad (34)$$

while the source term f includes the following term

$$f = \sum z_i(\bar{R}'_i + \bar{R}''_i) + P_e|\bar{\nabla}\phi| - \frac{\Gamma_r}{r}. \quad (35)$$

The last term in the previous expression accounts for the divergence operator in axisymmetric coordinates.

In addition to the above equations for the phase-field parameter, concentration of each ionic species, and solution potential, the **Solid Mechanics** interface can be used to implement the governing equation for mechanical equilibrium

$$\left\{ \begin{array}{lll} \bar{\nabla} \cdot \bar{\sigma} = \mathbf{0} & & \\ \bar{\mathbf{t}} = \mathbf{n} \cdot \bar{\sigma} = \bar{\mathbf{t}}^0 & \text{on } \partial\Omega_{\mathbf{t}} & \text{and} \quad \bar{\mathbf{u}} = \bar{\mathbf{u}}^0 \quad \text{on } \partial\Omega_{\mathbf{u}} \end{array} \right\}. \quad (36)$$

An extra term is added to the phase-field equation (following Eq. (22)) in the source term f

$$f = -\tau(\bar{\omega}g'(\phi) + h'(\phi)(\mathcal{F}_e^{\text{mech}} + \mathcal{F}_p^{\text{mech}})) - P_e|\bar{\nabla}\phi| - \frac{\Gamma_r}{r}. \quad (37)$$

The **Solid Mechanics** interface computes and gives access to the effective plastic strain ε^p and the hydrostatic stress σ_{h} . They affect the current density (Eq. (14)), which is included in the phase-field equation through the Peclet number P_e , Eqs. (24) and (25). To account for the degradation of the material stiffness associated with the evolution of the corrosion front ϕ , mechanical properties (λ and μ) are multiplied by the interpolation function $h(\phi)$.

3. Results

The results related to the above two case studies (buffer-free and buffer-controlled solutions) are given in this section for demonstration purposes. The interested reader is referred to the original paper [1] for more details and other case studies.

The predicted mass loss, the average concentration of Mg ions in solution, and pH levels are plotted against immersion time in Fig. 4, together with the experimental measurements obtained from the *in vitro* tests. The phase-field predictions and the test measurements are in good agreement for both air and 5% CO₂ environments. The phase-field predictions capture the experimental trends and accurately reproduce the measurements of mass loss, the average concentration of Mg ion in solution, and pH values for both air and 5% CO₂ environments, Fig. 4. Since the range of Cl⁻ ion concentrations considered in the present work does not influence the corrosion of the Mg wire, the predictions for the average concentration of Mg ions in solution and pH are only provided for the reference solution containing 104 mM NaCl. The inset in Fig. 4(c) portrays the distribution of Mg ions within the solution for the air environment at the final computational time. Two additional insets in Fig. 4(d) show the pH distribution in both environments at the final computational times. These insets indicate that a constant pH value of 10.5 is maintained throughout the domain in the air environment at the end of immersion. Albeit the bulk pH value is constrained in the

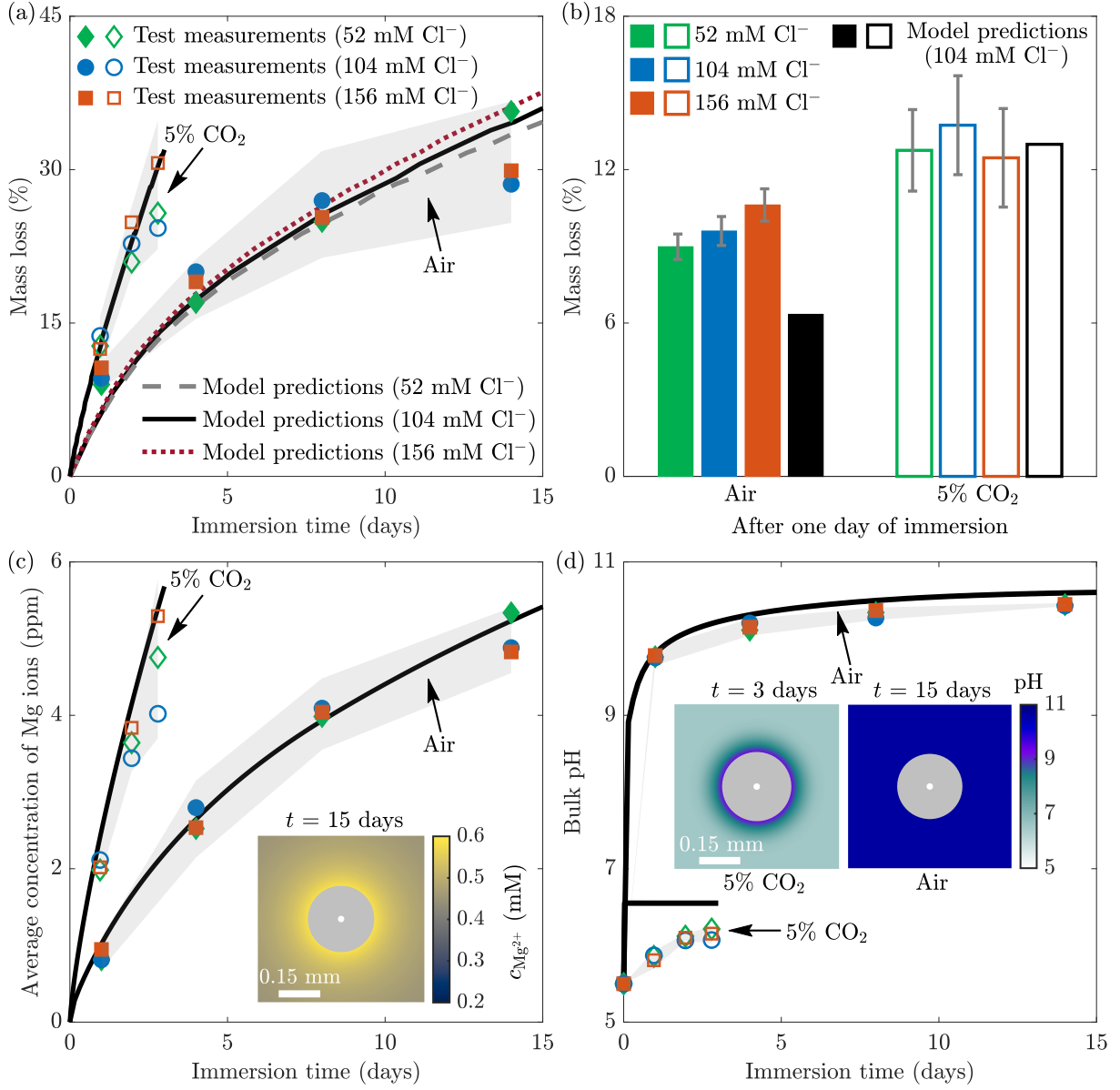


Figure 4: Comparison between experimental measurements and phase-field predictions for (a) mass loss, (b) mass loss after one day of immersion, (c) average concentration of Mg ions in solution, and (d) bulk pH. The light grey area stands for the standard deviation of the experiments considering data of all three NaCl solutions. The legends in the insets in (c) and (d) apply to the whole computational domain. The white point and grey area in the insets in (c) and (d) stand for the center and final cross-section of the Mg wire after degradation.

5% CO_2 environment, a nonuniform pH distribution is observed, with a significantly higher pH (around 9.2) near the interfacial area compared to the bulk solution. This significant difference in local (near wire surface) and bulk pH is physical and it has been observed before. A quantitative comparison is performed between experimental data and model predictions considering two metrics: mean absolute error (MAE) and root-mean-squared error (RMSE). The MAE values of 3.30%, 0.13, and 0.19 ppm are computed for mass loss, pH, and concentration of Mg^{2+} ions in the air environment. The corresponding values of 2.67%, 0.55, and 0.92 ppm are returned in the 5% CO_2 environment. The RMSE values between experimental and predicted values for mass loss, pH, and concentration of Mg^{2+} ions are 3.65%, 0.15, and 0.21 ppm in the air environment. The corresponding RMSE values of 4.27%, 0.56, and 1.07 ppm are obtained in the 5% CO_2 environment. The reported MAE and RMSE values are determined for the reference solution containing 104 mM NaCl. The model returns the experimental data using an exchange current density

$i_0 = 7.25 \times 10^{-11}$ A/cm² and a Damköhler number $D_a = 2500$. The returned exchange current density falls within the reported range of 10^{-6} A/cm² to 10^{-12} A/cm². The agreement between the model predictions and the experimental data on the concentration of Mg²⁺ ions in solution and the pH verifies that the Damköhler number is adequately chosen to accurately produce experimental measurements. The match with the experimental results for the concentration of Mg ions in solution and pH values in the 5% CO₂ environment indicates that the penalty coefficients \bar{k}_{pH} and \bar{k}_{MgCO_3} are suitably selected. A further increase in these coefficients would bring the model predictions closer to the experimental data at the cost of smaller time steps and longer computational times.

4. Concluding remarks

A finite element implementation of the phase-field model for assessing the degradation of bioabsorbable Mg implants in biological fluids developed by Kovacevic et al. (2025) is presented. The model is applicable to both buffer-free and buffer-regulated media. The dependence of corrosion on pH, chloride concentration, and mechanical fields is integrated into the model. The framework is validated against the *in vitro* tests on Mg wires in fluids with different pH and chlorine ion concentrations. Good agreement between experiments and simulations is attained.

The present document provides details of the model implementation in the software package COMSOL Multiphysics. Different case studies are explained in this document. The code developed is freely available at <https://mechmat.web.ox.ac.uk/codes>.

Acknowledgments

S.K. and E.M.-P. acknowledge financial support from UKRI's Future Leaders Fellowship program [Grant MR/V024124/1]. W.A. and J.L.L. acknowledge financial support from the BIOMET4D project (Smart 4D biodegradable metallic shape-shifting implants for dynamic tissue restoration) under the European Innovation Council Pathfinder Open call, Horizon Europe Research and Innovation program, grant agreement No. 101047008, and from the Spanish Research Agency through the grant PID2021-124389OB-C21. T.K.M. acknowledges the Newton International Fellowship (NIF/R1/221159) funded by The Royal Society. The authors would like to acknowledge the use of the University of Oxford Advanced Research Computing (ARC) facility in carrying out this work (<http://dx.doi.org/10.5281/zenodo.22558>).

References

- [1] S. Kovacevic, W. Ali, T. K. Mandal, E. Martínez-Pañeda, J. LLorca, Impact of pH and chloride content on the biodegradation of magnesium alloys for medical implants: An in vitro and phase-field study, *Acta Biomaterialia* 198 (2025) 546–565. doi:<https://doi.org/10.1016/j.actbio.2025.03.034>.
- [2] COMSOL Multiphysics v. 6.1. www.comsol.com. COMSOL AB, Stockholm, Sweden.
- [3] COMSOL Multiphysics v. 6.1. Reference Manual.